CHEMISTRY OF MATERIALS

Open Access
This article is licensed under CC-BY 4.0

pubs.acs.org/cm
Article

Isoreticular Expansion in Porous Aluminum(III) and Gallium(III) Phosphonates: Synthesis, Structure, and Properties

Jennifer Theissen, Marvin Radke, Sebastian Mangelsen, Elien Derveaux, Roberth Mateo Narváez Adams, Tobias Wagner, Jasper Lopau, Christian Näther, Christian Nelle, Jörn Struve, Felix Steinke, Jesús Gándara Loe, Nick Gys, Tom Hauffman, Michael Tiemann, Frederik Tielens, Peter Adriaensens, Sebastian Henke, Wouter Marchal,* Rob Ameloot,* and Norbert Stock*

Cite This: *Chem. Mater.* 2026, 38, 8463−8475

Read Online

ACCESS | Metrics & More | Article Recommendations | Supporting Information

ABSTRACT: We report the synthesis, structural elucidation, and establishment of structure−property relationships for two metal−organic frameworks (MOFs), $[M(OH)(H_2BPD)]\cdot xH_2O$ (M = Al^{3+}, Ga^{3+}, x = 11−13), denoted as M-CAU-67, employing the ditopic linker molecule *N,N′*-4,4′ bipiperidine bis(methylenephosphonic acid) (H_4BPD). The title compounds can be synthesized on a milligram scale under hydrothermal conditions, while gram-scale synthesis was realized under reflux conditions. Single-crystal X-ray diffraction (SCXRD) revealed an isoreticular, expanded MIL-91 type structure, representing a rare case of isoreticular expansion in porous metal phosphonates. The framework structure was confirmed by Rietveld refinement against powder X-ray diffraction (PXRD) data and further validated by solid-state NMR spectroscopy (^{31}P MAS, ^{27}Al 3Q MAS). Solvent-exchange experiments and variable-humidity/temperature PXRD data revealed high framework flexibility. The compounds show permanent microporosity and a complex, polarity- and size-dependent sorption behavior toward gases and vapors.

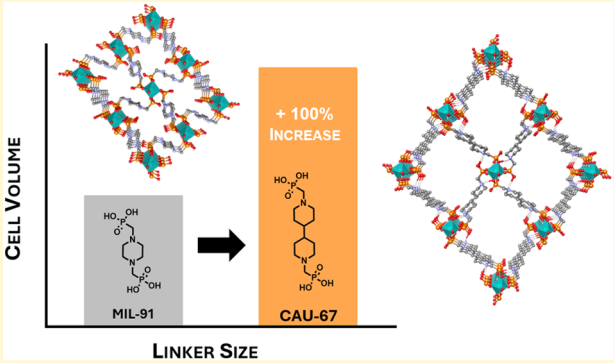

INTRODUCTION

Metal−organic frameworks (MOFs) have emerged as a versatile class of materials, due to their modular construction from inorganic building units (IBUs), such as metal ions or metal−oxygen clusters, and organic linker molecules, commonly carboxylates or imidazolates.[1,2] Their remarkable structural diversity and functional versatility have led to a wide range of applications,[3] including proton conductivity,[4,5] ion exchange,[6] catalysis,[7,8] water harvesting,[9] as well as gas storage and separation.[10] In contrast to the vast number of carboxylate- and imidazolate-based MOFs, phosphonate-based frameworks remain underexplored: Only 2.29% of the structures in the MOF subset of the Cambridge Structural Database[11] (CSD; July 2026) are derived from phosphonic acids. Porous metal phosphonates (MPs) offer distinct advantages, including exceptional thermal[12,13] and chemical[5,8] stability, attributed to strong metal-phosphonate (P−O−M) bonds and the multiple coordination modes of phosphonate ligands.[3,14,15] The synthesis of crystalline, porous MPs remains challenging due to various reasons:[3,16] (1) uncontrolled nucleation: controlled self-assembly during nucleation and crystallization is impeded because of the stronger P−O−M bonds compared to C−O−M interactions, resulting in the fast precipitation of amorphous or poorly crystalline materials;[17] (2) hard-to-predict coordination behavior due to the variable (de)protonation states and coordination modes of the phosphonate group;[14,18] (3) general tendency toward dense, nonporous layer formation;[14,18] (4) limited commercial availability of phosphonic acid linkers and, therefore, often requiring their multistep synthesis. These challenges are reflected in the small number of reported crystalline and porous phosphonate MOFs. For instance, only eight crystalline and porous aluminum MPs have been reported over the past three decades (SI, Section 1, Tabel S1). Until the early 2000s, reports of porous MPs remained relatively scarce.[15] Prominent early examples employing monophosphonic acids were β-$Cu(O_3P\text{-}CH_3)$,[19] $(H_3O)[(V_3O_4)(H_2O)(O_3P\text{-}Ph)_3]$,[20] AlMePO-$\alpha$[21] and -$\beta$[21] ($Al_2(O_3PCH_3)_3$). While the pore size of β-$Cu(O_3P\text{-}CH_3)$ is very small (ca. 2.8 Å), limiting the adsorption

Received: May 8, 2026
Revised: July 20, 2026
Accepted: July 22, 2026
Published: August 3, 2026

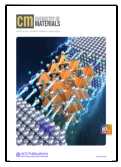

ACS Publications
© 2026 The Authors. Published by American Chemical Society

https://doi.org/10.1021/acs.chemmater.6c01336
Chem. Mater. 2026, 38, 8463−8475

Downloaded from pubs.acs.org/cmatex/article-pdf/38/16/8463/66357783/acs.chemmater.6c01336.pdf by IMEC VZW user on 28 October 2026

of common probe molecules, the pores of the other early metal phosphonates are sufficiently large to host small guest molecules such as nitrogen or water. The use of ditopic phosphonic acids to link adjacent layers often resulted in dense, nonporous structures. Strategies involving mixed-linker systems, including monophosphonates or phosphates, introduced some porosity but often at the expense of crystallinity and broad pore-size distributions due to the stochastic nature of defect formation.[22−24] More refined approaches, such as the "column-with-base" strategy developed by Alberti et al.,[22] leveraged aromatic diphosphonates bearing sterically demanding substituents (−CH_3, −OH, −COOH) close to the phosphonate moieties to achieve well-defined porous structures with improved crystallinity and narrower pore size distributions.[22,25] The incorporation of additional functional groups, such as tertiary amines in piperazine- and bipiperidine-derived linkers, further expanded the porous MP landscape, resulting in a series of frameworks reported throughout the early 2000s and 2010s. In 2006, a milestone was reached when Serre et al.[26] reported MIL-91, the first porous metal phosphonate synthesized from *N,N′*-piperazine-bis(methylene phosphonic acid) (H_4PMP), incorporating tri- and tetravalent metal cations (Al^{3+} and Ti^{4+}).[26] MIL-91 exhibits well-defined, narrow pores with a cross-section of ∼3.5 × 4.0 $Å^2$ and notable CO_2 uptake, thereby highlighting the potential of porous MPs in gas storage and separation.[26,27] Isostructural phosphonate frameworks, i.e., frameworks with the same structure but different metal ions, have also been reported. Examples include STA-12[28] and -16,[28] CAU-53,[29] CAU-60,[30] and CALF-41.[31] When metals of different oxidation states are involved, charge compensation is usually achieved by varying degrees of framework protonation, as in MIL-91.[26] Isostructural phases can also be obtained by employing either the phosphonic acid or its monoester derivative, as observed for CALF-33.[32]

To address the limitations of narrow pore structures, researchers have turned to isoreticular chemistry, i.e., systematic linker extension while retaining the topology.[33,34] While the isoreticular approach has led to major progress in carboxylate MOFs, its application to porous MPs has been hindered by the unpredictability of phosphonate group coordination.[35] Therefore, reports of isoreticular expansion via increased linker size are extremely rare in porous MPs, with some alkyl bisphosphonates of divalent metal ions as reported examples (STA-12 and -16).[14,36,28] Notably, the STA-12/-16 system provides an important reference case, since it also employs piperazine- and bipiperidine-based bisphosphonate linkers, but displays a different framework response upon linker extension. In contrast, the use of trivalent metal ions often leads to nonporous or poorly crystalline compounds.[14,37,38] Recently, a mini-review highlighted the structural similarities among IBUs in porous MPs and emphasized the challenge of identifying synthesis conditions that yield the same IBU for different phosphonic acids.[39] As a result, progress in expanding the structural and functional diversity of porous MPs remains limited.

In this work, we extend the concept of isoreticular expansion by reporting the isostructural M-CAU-67 (M = Al^{3+}, Ga^{3+}) compounds, based on the H_4BPD linker, an extended H_4PMP analog. The framework adopts an expanded MIL-91-type structure. Their discovery was achieved via a high-throughput approach (SI, Section 3.3), and phase-pure compounds were obtained under different synthetic conditions. The frameworks exhibit reversible structural flexibility in response to hydration and dehydration, as revealed by variable-temperature (VT-) and variable-humidity (RH-) PXRD measurements. Al- and Ga-CAU-67 exhibit similar structural and textural behavior under the conditions explored. Therefore, Al-CAU-67 was selected as the primary case study and is fully characterized in the manuscript, while Ga-CAU-67 is described in detail in the Supporting Information (SI).

■ EXPERIMENTAL SECTION

Materials and Methods

All commercially available chemicals were used without further purification. Aluminum(III)chloride hexahydrate (≥99%) and phosphorous acid (99%) were purchased from Sigma-Aldrich. Gallium(III)chloride (anhydr.) was purchased from abcr GmbH. Sodium hydroxide (99%) was purchased from ORG Laborchemie GmbH. Hydrobromic acid, 48 wt % aqueous solution (p.a.) was purchased from Honeywell International Inc. 4,4′-bipiperidine dihydrochloride (98%) was purchased from BLD Pharmatech GmbH. Formaldehyde, 35 wt % aqueous solutions (stabilized with 7−8% MeOH), methanol (99%), ethanol (>99.8%), dichloromethane, stabilized with amylene (≥99.8%, dry), were purchased from Thermo Fisher Scientific Inc. Deionized water was produced in-house through ion exchange.

Solvothermal syntheses were performed in custom-made steel autoclaves with PTFE inserts with total volumes ranging from 2 to 20 mL. Microwave-assisted solvothermal syntheses were performed with Biotage Initiator + in PTFE-capped 10−20 mL glass vials under continuous stirring. Reflux synthesis was carried out in a round-bottom flask and a Dimroth condenser made of Duran glass. A PTFE-coated stir bar was used. A magnetic heating stirrer with an oil bath was used to heat the round-bottom flask. The standard stirring speed was 600 rpm.

Data collection for SCXRD was performed at 100 and 293 K using a XtaLAB Synergy Dualflex, HyPix diffractometer from Rigaku using Cu-radiation (λ = 1.5418 Å). PXRD data for structure refinements were collected on a STOE Stadi MP instrument equipped with a MYTHEN 1K detector (Cu Kα_1-radiation, λ = 1.5406 Å). A flat transmission sample holder was used for data acquisition. Temperature-dependent and variable relative-humidity in situ XRD measurements were performed using a Malvern Panalytical Empyrean diffractometer equipped with an Anton Paar TTK 600 chamber, nonmonochromated Cu radiation (Cu $K_{\alpha1}$ = 1.5406 Å, Cu $K_{\alpha2}$ = 1.5443 Å), and a PIXcel 3D 1 × 1 solid-state pixel detector.

Volumetric sorption measurements were performed using a BEL Japan Inc. BELSORP-max at different temperatures (N_2 at 77 K, Ar at 87 K, H_2O, MeOH, EtOH, 1-BuOH, and Toluene at 298 K). Volumetric CO_2 sorption measurements were carried out at 298 K using a BEL Japan Inc. BELSORP MiniX. Before the measurements, the samples were dried and degassed for 2 h under reduced pressure ($p < 10^{-2}$ kPa) at 80 °C. If other activation conditions were used, they are mentioned in the described results.

Thermogravimetric (TG) measurements in conjunction with differential scanning calorimetry (DSC) were carried out in dry air or nitrogen atmosphere using a Linseis STA PT 1600 (heating rate = 4 K min^{-1}, airflow = 6 L h^{-1}). The DSC measurements were performed under nitrogen gas flow (50 mL min^{-1}) using a TA Instruments DSC25 with aluminum sample pans. The measurements were performed at heating and cooling rates of ±10 °C min^{-1}, with a series of three up-scans and two down-scans over the range from approximately 30 to 300 °C.

DRIFTS measurements were conducted employing a Bruker Vertex 70 FTIR spectrometer, a Harrick Scientific Products Praying Mantis diffuse reflection accessory, and a Harrick Scientific Products Praying Mantis high-temperature reaction chamber. A resolution of 4 cm^{-1} was used, and for each spectrum, 200 scans were accumulated. Measurements were performed at different temperatures under air after a 5 min stabilization time. The sample holder contained a 15 wt % diluted sample in KBr.

Downloaded from pubs.acs.org/cmatex/article-pdf/38/16/8463/66357783/acs.chemmater.6c01336.pdf by IMEC VZW user on 28 October 2026

https://doi.org/10.1021/acs.chemmater.6c01336
Chem. Mater. 2026, 38, 8463−8475

Scanning electron microscopy (SEM) images of the samples were acquired using a Hitachi SU8700. The SEM offers different detectors, e.g., an in-column secondary electron (SE) upper detector (UD), an in-column backscattered electron (BSE) middle detector (MD), and an Everhart-Thornley detector in the chamber (SE/BSE, lower detector LD). EDX analyses were performed with an Oxford EDX Ultim Max 100 detector. The samples were prepared with carbon pads on an aluminum pin-mount sample holder.

Solid-state NMR (ssNMR) spectra were acquired on a JEOL ECZ600R 600 MHz spectrometer (14.1 T) equipped with a 3.2 mm probe. Unless otherwise noted, all spectra were recorded under ambient temperature. The KH_2PO_4 signal was used to calibrate the phosphorus chemical shift scale (3.9 ppm), while the $AlCl_3$ signal was used to calibrate the aluminum chemical shift scale (0 ppm). Acquisition parameters used were (i) for ^{31}P NMR: Magic-angle-spinning (MAS) rate of 18 kHz, a spectral width of 60 kHz, a 90° pulse length of 3.4 μs, a relaxation delay of 60 s, an acquisition time of 9.5 ms and between 70 and 100 accumulations; (ii) for the central transition selective ^{27}Al NMR: MAS rate of 18 kHz, a spectral width of 100 kHz, a CT-selective 90° pulse length of 21 μs with a field strength of 11.9 kHz, a relaxation delay of 0.3 s, an acquisition time of 8.7 ms and between 250 and 300 accumulations. Triple quantum MAS (3Q MAS) spectra were recorded at a MAS rate of 18 kHz, a spectral width of 60 kHz, using a relaxation delay of 0.3 s, an acquisition time of 8.7 ms, and between 350 and 450 accumulations. The Split-t1-based pulse sequence with Z filter comprises a hard 2.6 μs pulse at 96.2 kHz and a selective 21 μs pulse. Pulse lengths for fast amplitude modulation (FAM) conditions were iteratively optimized to enhance sensitivity.

Proton conductivity measurements were performed on polycrystalline samples prepared in the form of pellets with thicknesses ranging from 0.5 mm to 1 mm and a radius of 6.5 mm. The conductivity of the samples was measured using impedance spectroscopy with a Novocontrol α-A high-performance frequency analyzer in a frequency range of 1 Hz to 4.6 MHz and an applied voltage of 0.1 V. The samples were placed between gold-plated electrodes in two-wire mode. Humidity-dependent measurements were carried out by placing the cell in an Espec SH-242 climate chamber, which enabled independent control of temperature and humidity. The samples were allowed to equilibrate to the desired humidity (60, 70, 80, and 90% RH) and temperature (25, 30, 40, and 50 °C) for 24 h. Starting at the lowest humidity, the temperature was raised before the humidity was increased.

Additional information on the experimental methods is given in the SI Section 2.1.

Synthesis

The aluminum-based framework Al-CAU-67, $[Al(OH)(H_2BPD)]\cdot xH_2O$ (x = 11−13), was discovered through a systematic high-throughput investigation, involving $AlCl_3$, the linker H_4BPD, NaOH as pH modulator, and multiple temperature−time protocols (Figure 1). The linker molecule H_4BPD was synthesized using a modified procedure from the literature.[28] Details are given in the Supporting Information (SI Section 3.2).

Phase-pure formation of highly crystalline Al-CAU-67 was achieved by combining H_4BPD, water, aqueous solutions of NaOH and $AlCl_3$ in a molar ratio of $AlCl_3/H_4BPD/NaOH$ = 1.2:1:3. Hydrothermal synthesis at 135 °C under continuous stirring in glass vessels with or without microwave-assisted heating and without stirring in PTFE-lined steel autoclaves yielded the compound as a colorless, microcrystalline powder with various crystallite sizes and shapes, depending on the synthesis method and modulator use (Figure 1, conditions in SI Section 3.4 and SEM images in SI Section S4.6). Notably, scale-up was readily achieved under reflux conditions in a round-bottom flask (250 mL), yielding up to 2.3 g of product per batch. Analogous synthesis procedures yielded the gallium analog, Ga-CAU-67; detailed data for this compound, which exhibits similar properties, are provided, together with the comprehensive analytical data for Al-CAU-67, in SI Section 4.

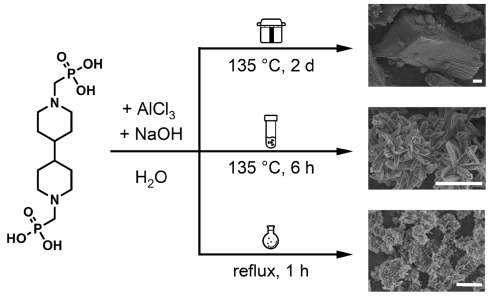

Figure 1. Summary of the synthesis conditions resulting in the formation of Al-CAU-67; $[Al(OH)(H_2BPD)]\cdot xH_2O$. Different synthesis methods led to different particle morphologies. Solvothermal synthesis at 135 °C for 2 d in PTFE lined steel autoclaves (middle, top) led to irregularly shaped block-like crystallites; microwave-assisted synthesis at 135 °C with constant stirring for 6 h in glass vials (middle, middle) led to homogeneous block-shaped crystallites; and reflux-based synthesis in a round-bottom flask with constant stirring for 1 h (middle, bottom) led to very small, regularly shaped needles. The scale bar corresponds to 5 μm.

Samples collected immediately after the synthesis are denoted as **AS** (as-synthesized). To render the pores accessible and prevent pore collapse upon water removal, solvent exchange was conducted; samples subjected to this treatment are denoted as **SE** (solvent-exchanged). Thermally activated samples are denoted as **Act**. Samples treated by refluxing the material in water are referred to as **Reflux**. Regeneration of the crystalline M-CAU-67 phase after thermal treatment was achieved by exposing the dehydrated material for at least 30 h to 75% RH or refluxing in water for 1 h; these samples are denoted as **Rehydration**. Unless otherwise specified, all characterizations were performed on samples obtained from microwave-assisted syntheses and were subjected to a reflux treatment.

■ RESULTS AND DISCUSSION

Structure Determination and Description

Although Al-CAU-67 was obtained as single crystals suitable for SCXRD, the disordered nature of the water molecules in the pores prevented their localization in the electron density map. Therefore, their contribution was removed to refine the SC data (SI Section 4.1). Since this solvent contribution is present in the hydrated bulk material, its omission led to discrepancies between the observed and calculated intensities in the PXRD pattern (SI Section 4.1). To account for the average scattering contribution of the pore water in the hydrated bulk phase, the crystal structure was refined against PXRD data collected at RT (Figure 2A and Table 1). Based on the results of elemental and TG analyses of the same sample (SI Section 4.3), 11 additional oxygen atoms corresponding to noncoordinating water molecules were introduced and subjected to global optimization using simulated annealing,[40] as implemented in TOPAS Academic.[41] Repeatedly, minima were found in which all solvent molecules are located in the pore, not colliding with any of the framework atoms. No constraints had to be applied. These sites are regarded as representative average oxygen positions of disordered pore water; hydrogen atoms were not added nor refined. Further, the linker molecules, modeled as rigid bodies with a variable torsion angle of the phosphonate group about the C−N bond, were refined. The Rietveld refinement resulted in only minor positional changes compared to the single-crystal structure determination and is in good agreement with the measured PXRD data (Figure 2A). Refinement against pair distribution

Downloaded from pubs.acs.org/cmatex/article-pdf/38/16/8463/66357783/acs.chemmater.6c01336.pdf by IMEC VZW user on 28 October 2026

https://doi.org/10.1021/acs.chemmater.6c01336
Chem. Mater. 2026, 38, 8463−8475

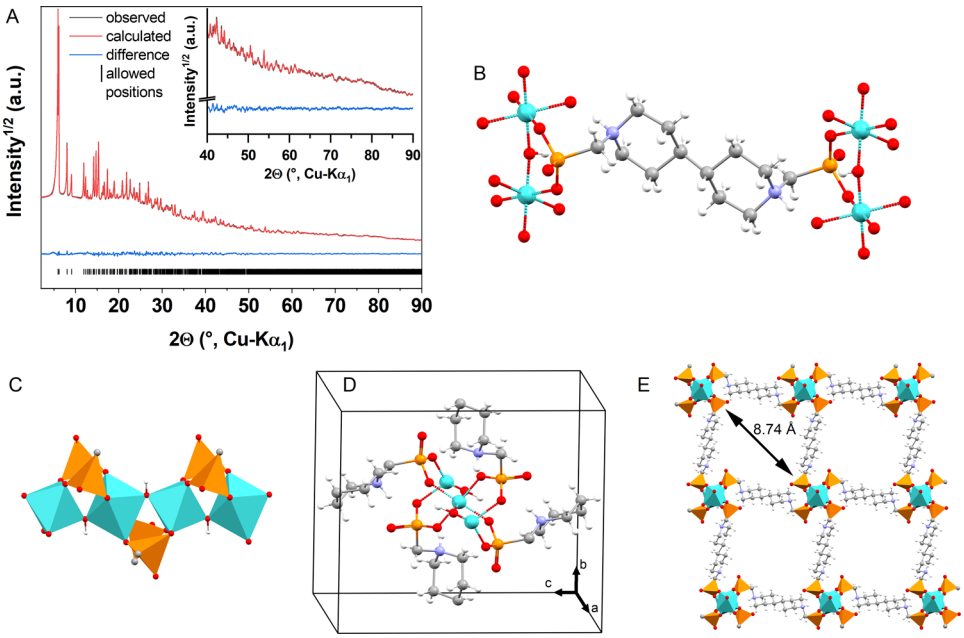

Figure 2. (A) Final Rietveld plot of Al-CAU-67-AS. The measured PXRD pattern is shown in black, and the calculated one in red. The difference between the calculated and measured PXRD patterns is shown in blue. Permitted reflection positions are shown as black vertical lines. The *y*-axis is scaled using square-root scaling to make differences more visible. (B) Connectivity of a linker molecule to the aluminum ions. (C) IBU formed by the trans-corner-sharing AlO_6- and CPO_3-polyhedra along the *a*-axis with phosphonate-groups originating from different linker molecules. (D) unit cell and (E) pores of CAU-67 seen along the *a*-axis, oxygen atoms representing the guest molecules omitted for clarity. General color scheme: Al = turquoise, P = orange, O = red, N = purple, C = gray, H = white.

Table 1. Summary of Crystallographic Data of Al-CAU-67-AS, $[Al(OH)(H_2BPD)]\cdot 11H_2O$, Obtained by Rietveld Refinement Against PXRD Data[a]

Parameter	Value	Parameter	Value
Empirical formula	$[Al(OH)(C_{12}H_{24}N_2O_6P_2)]\cdot 11H_2O$	α/°	82.521(3)
Formula weight/g mol^{-1}	596.44	β/°	85.9141(18)
Temperature/K	293	γ/°	79.119(3)
Crystal system	triclinic	V/Å^3	1463.67(6)
Space group	$P\bar{1}$	R_{Bragg}/%	0.641
a/Å	6.83391(12)	R_p/%	1.56
b/Å	14.6963(4)	R_{exp}/%	4.86
c/Å	14.9849(4)	R_{wp}/%	2.03
		GoF	0.419

[a]The low GoF value is a consequence of the comparatively large R_{exp} value and is therefore attributed to the conservative weighting of the PXRD data; the structural model is independently supported by SCXRD and ssNMR.

function (PDF) data revealed an overall similar framework structure, with differences attributable to disordered solvent molecules (SI Section 4.1.3).

Al-CAU-67-AS, $[Al(OH)(H_2BPD)]\cdot 11H_2O$, crystallizes in a structure that is isoreticular to Al-MIL-91.[42] Structural details are shown in Figure 2. The asymmetric unit contains two Al^{3+} cations, one situated at the center of the unit cell and the other at the center of the *bc*-face, connected by a bridging (μ-)OH group. Two crystallographically independent linker molecules are oriented parallel to the *b*- and *c*-axes on general positions. Each Al^{3+} cation is 6-fold coordinated by four oxygen atoms from four different phosphonate groups and two hydroxide ions, forming the IBU. The hydroxide ions (μ-OH) connect adjacent Al^{3+} ions, forming an infinite chain of *trans*-corner-sharing AlO_6-polyhedra extending along the *a*-axis direction (Figure 2C). Each H_2BPD^{2-} linker bridges four Al^{3+} ions via its phosphonate groups, with each phosphonate group coordinating two Al^{3+} ions within the same chain in a coordination mode described as [2.110] in Harris notation (Figure 2B).[43]

Two crystallographically independent linker molecules interconnect the infinite chains along the *b*- and *c*-axes, forming a three-dimensional coordination network. The unidirectional rhombic channels of the hydrated CAU-67 show a limiting diameter of 8.74 Å and a maximum pore diameter of 9.26 Å (Figure 2E) as determined by PoreBlazer.[44−46] The topology of CAU-67, as well as MIL-91, is also observed in metal carboxylates with the MIL-53-type structure. Depending on the representation of the vertices, the framework can be described either by an **sra** (4,4-net), **rna** (3,6-net), or **bqp** (4,6-net) topology.[47,48] In the *Cheetham*[49] notation for hybrid solids, the structures of CAU-67, MIL-91, and MIL-53 can be described as one-dimensionally connected IBUs that are further linked in two dimensions by the organic linker, resulting in a three-dimensional framework denoted as I^1O^2. The linker molecule is 2-fold protonated, as observed in

https://doi.org/10.1021/acs.chemmater.6c01336
Chem. Mater. 2026, 38, 8463−8475

Downloaded from pubs.acs.org/cmatex/article-pdf/38/16/8463/6635778 3/acs.chemmater.6c01336.pdf by IMEC VZW user on 28 October 2026

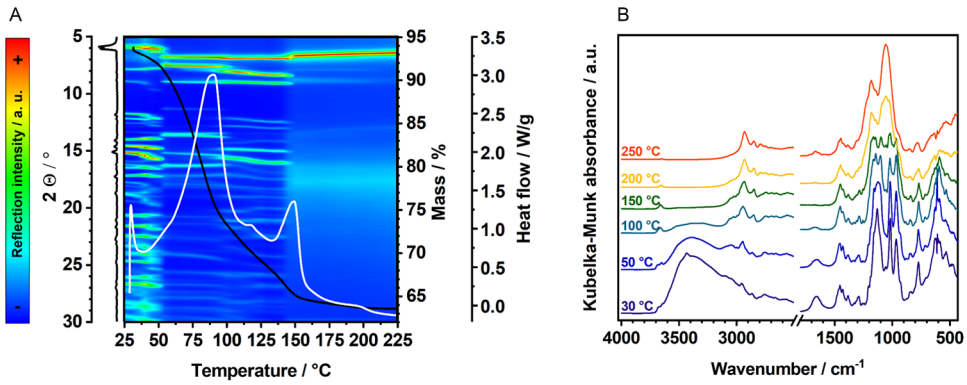

Figure 3. (A) Combination of the results of the VT-PXRD, TGA, and DSC measurements. Contour plot of reflection intensity of VT-PXRD (color scale) as a function of 2Θ and temperature (*y*-axis, left). The black line represents the TG curve (on the first, right *y*-axis), showing the removal of water molecules from the pores. The DSC signal (white curve, second right *y*-axis) shows the heat flow, exothermically down. (B) DRIFT spectra recorded at selected temperatures (offset for clarity).

Al-MIL-91.[26] These protons are located at the tertiary nitrogen atoms of the bipiperidine rings. The protonation of the tertiary nitrogen atoms in CAU-67 is supported by SCXRD, FTIR, and DRIFT spectroscopy (SI Sections 4.1, 4.5, and 4.12). The tertiary nitrogen atoms form hydrogen bonds with the phosphonate oxygen atoms of neighboring linker molecules, which contribute to additional stabilization of the structure. Two distinct donor−acceptor distances are observed: (1) N1−H···O12 = P11 with an N1···O12 separation of 2.788(14) Å, and (2) N11−H···O2−P1 with a N11···O2 separation of 2.844(10) Å. Similar motifs are found in Al-MIL-91, where slightly shorter hydrogen-bond lengths (2.564(9) and 2.597(7) Å) have been proposed to contribute to the framework rigidity.[26,42] Similar hydrogen bond interactions have also been reported in the [$ZrF_2(H_2PMP)$] (d(O···N) = 2.611(2) Å)[50] and the α-PCMOF21-Cl framework (d(O···N) = 2.733 Å).[51]

The framework structure differs from that of the STA-12/STA-16 system, although both families are based on the same piperazine- and bipiperidine-derived bisphosphonate linker molecules.[28] In the STA-12/STA-16 system, the nitrogen atoms of the linker are directly involved in the metal coordination, resulting in MO_5N coordination polyhedra that form edge-sharing helical inorganic units.[28] The organic linker backbone is therefore an integral part of the inorganic building unit, while additional phosphonate bridges between neighboring metal centers further constrain the framework.[28] In contrast, MIL-91[26,42] and CAU-67 are constructed from μ-OH-bridged MO_6 chains. Here, the linker nitrogen atoms are protonated and do not participate in metal coordination. Instead, they form hydrogen bonds with phosphonate oxygen atoms of neighboring linker molecules. Consequently, the organic linker is not incorporated directly into the IBU but instead acts more as a flexible spacer between adjacent inorganic chains. This weaker coupling is expected to give greater conformational flexibility, the implications of which are discussed later in this work.

Thermal Properties

The thermal behavior of Al-CAU-67 was examined using variable-temperature PXRD (VT-PXRD), thermogravimetric and differential thermal analysis (TGA-DTA), differential scanning calorimetry (DSC), and temperature-dependent diffuse reflectance infrared Fourier transform spectroscopy (TD-DRIFTS).

Mass losses associated with the removal of guest molecules and framework decomposition were monitored by TG analysis. The TG data of Al-CAU-67 (Figure 3A, black line and SI Section 4.3) exhibited a small weight loss during equilibration at 30 °C under N_2 flow, followed by a two-step mass loss accompanied by endothermic events in the DSC curve (Figure 3A, white line and SI Section 4.4) indicating the presence of physisorbed water residing in the one-dimensional channels, with T_{end} = 90 °C ($\Delta H \approx$ 172 kJ mol^{-1}) and T_{end} = 150 °C ($\Delta H \approx$ 38.4 kJ mol^{-1}), respectively (SI section 4.4). The combined mass loss (Δm_{sum} = 36%) corresponds to the release of ≈13 H_2O molecules per formula unit ($\Delta m_{calc.}$ = 37%). Interparticle condensation of adsorbed water molecules within the bulk material results in a greater total mass loss than expected from the Rietveld refinement, as observed in other MOFs with high water uptake capacity.[52] VT-PXRD (Figure 3A, contour plot) revealed a series of structural transformations of Al-CAU-67 at approximately 40, 60, 95, 120, and 150 °C, which correlate with the dehydration events evidenced in the TG and DSC curves (Figure 3A, black line). Starting at 150 °C, the TG curve exhibited a plateau, which, in combination with VT-PXRD data (Figure 3A and SI Section 4.9), indicates the formation of an anhydrous framework that remains thermally stable in this temperature range. Above 361 °C, the sample appeared to decompose (SI, Section 4.3.3). We hypothesize that the observed transformations originate from the reorganization and gradual loss of physisorbed water, followed by framework contraction upon guest removal to minimize empty pore volume. Upon dehydration, most reflections shifted to higher 2θ values, consistent with unit-cell contraction and the formation of a "narrow-pore phase" that persists up to 150 °C (SI Section 4.9). Above that temperature, only a few reflections at low angles and diffuse scattering could be observed (Figure 3A and SI Section 4.9), pointing to a loss of the long-range order of the network.

Temperature-dependent DRIFTS measurements provide additional support for the proposed dehydration mechanism (Figure 3B). The bridging μ-OH stretching vibration[53] at 3665 cm^{-1} remained visible up to 250 °C, confirming the integrity of the inorganic building units despite loss of long-range order above 150 °C. The N−H stretching vibration around 2850 cm^{-1}, assigned to the protonated tertiary nitrogen atom of the linker molecule,[53] is visible over the entire temperature range, indicating that deprotonation of the tertiary nitrogen atoms

https://doi.org/10.1021/acs.chemmater.6c01336
Chem. Mater. 2026, 38, 8463−8475

Downloaded from pubs.acs.org/cmatex/article-pdf/38/16/8463/66357783/acs.chemmater.6c01336.pdf by IMEC VZW user on 28 October 2026

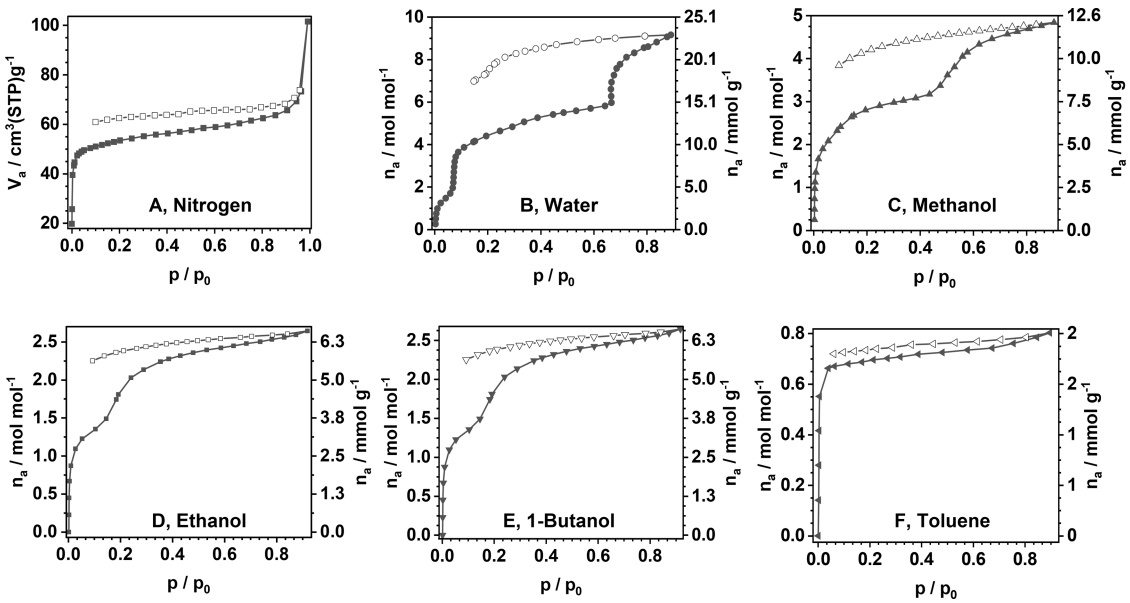

Figure 4. Sorption isotherms of Al-CAU-67-SE using (A) Nitrogen gas at 77 K, (B) water vapor at 298 K, (C) MeOH vapor at 298 K, (D) EtOH vapor at 298 K, (E) 1-BuOH vapor at 298 K, and (F) Toluene vapor at 298 K. The adsorption (filled symbols) and desorption (open symbols) branches of the isotherms are shown. n_a given in adsorbed molecules per formula unit (mol mol^{-1}) and adsorbed molecules per gram (mmol g^{-1}).

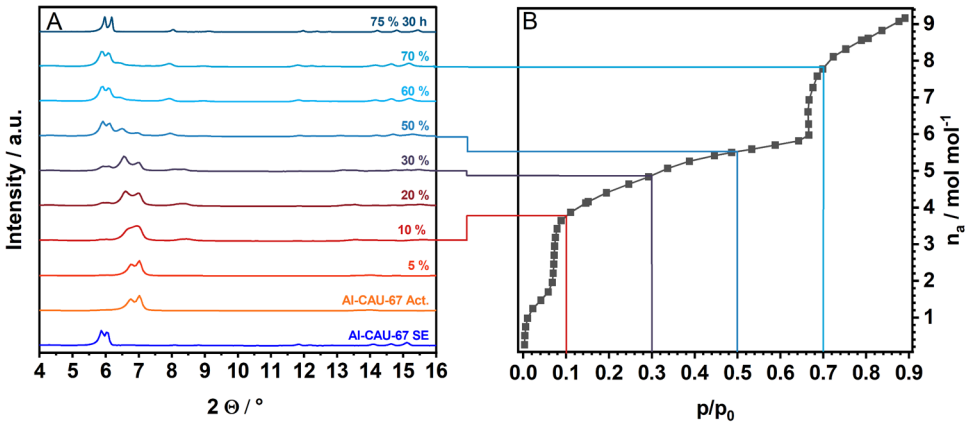

Figure 5. (A) Humidity-dependent in situ PXRD data and (B) water-vapor adsorption isotherm of Al-CAU-67-SE, i.e., Al-CAU-67 loaded with DCM molecules. Before measurement, the sample was activated under dry N_2 (80 °C, 3 h) to obtain Al-CAU-67 Act. RH values for in situ PXRD were selected to correspond to characteristic regions of the adsorption isotherm.

does not occur and that the phosphonate groups remained coordinated to the aluminum ions. With progressive dehydration, the water-related absorption bands at 3350 cm^{-1} (O−H stretching)[53] and 1655 cm^{-1} (H−O−H bending)[53] diminish and disappear above 150 °C, consistent with the formation of a dehydrated phase. The merging and broadening of vibrational modes in the fingerprint region above 150 °C further reflect the loss of long-range order and are attributed to decreased local structural order.

In contrast, Al-MIL-91 undergoes only minor unit-cell changes upon heating.[26] This pronounced structural rigidity is attributed to strong hydrogen bonds between the phosphonate groups and the tertiary nitrogen atoms of the piperazine-based linker, as evidenced by the short hydrogen-bond length.[26] For CAU-67, the major changes in the PXRD pattern upon the loss of guest molecules are probably linked to the higher conformational flexibility of the linker molecule and the weaker hydrogen bonding.

Sorption Properties

The host−guest interactions of Al-CAU-67 with different probe molecules were also investigated (Figure 4). An activated AS sample (80 °C, $p < 10^{-2}$ kPa, 16 h) showed a negligible N_2 uptake at 77 K, most likely due to framework collapse caused by capillary forces during removal of the water molecules (SI Section 4.7). To prevent collapse, a sequential solvent-exchange step was carried out using MeOH, EtOH, and DCM, and the samples were kept in DCM until the final activation step (80 °C, $p < 10^{-2}$ kPa). N_2 isotherms were recorded at 77 K to determine the BET surface area.[54] Water, MeOH, EtOH, 1-BuOH, and toluene isotherms recorded at 298 K were used to investigate vapor uptake. Additional sorption measurements were performed with CO_2 at 298 K, and Ar at 87 K. Al-CAU-67 was found to be porous to all tested adsorbents (Figure 4 and SI Section 4.7).

The N_2 isotherm of Al-CAU-67-SE exhibits Type-I behavior with a BET surface area of 205 m^2 g^{-1}, markedly lower than the theoretical value of 1084 m^2 g^{-1} calculated with

https://doi.org/10.1021/acs.chemmater.6c01336
Chem. Mater. 2026, 38, 8463−8475

Downloaded from pubs.acs.org/cmatex/article-pdf/38/16/8463/66357783/acs.chemmater.6c01336.pdf by IMEC VZW user on 28 October 2026

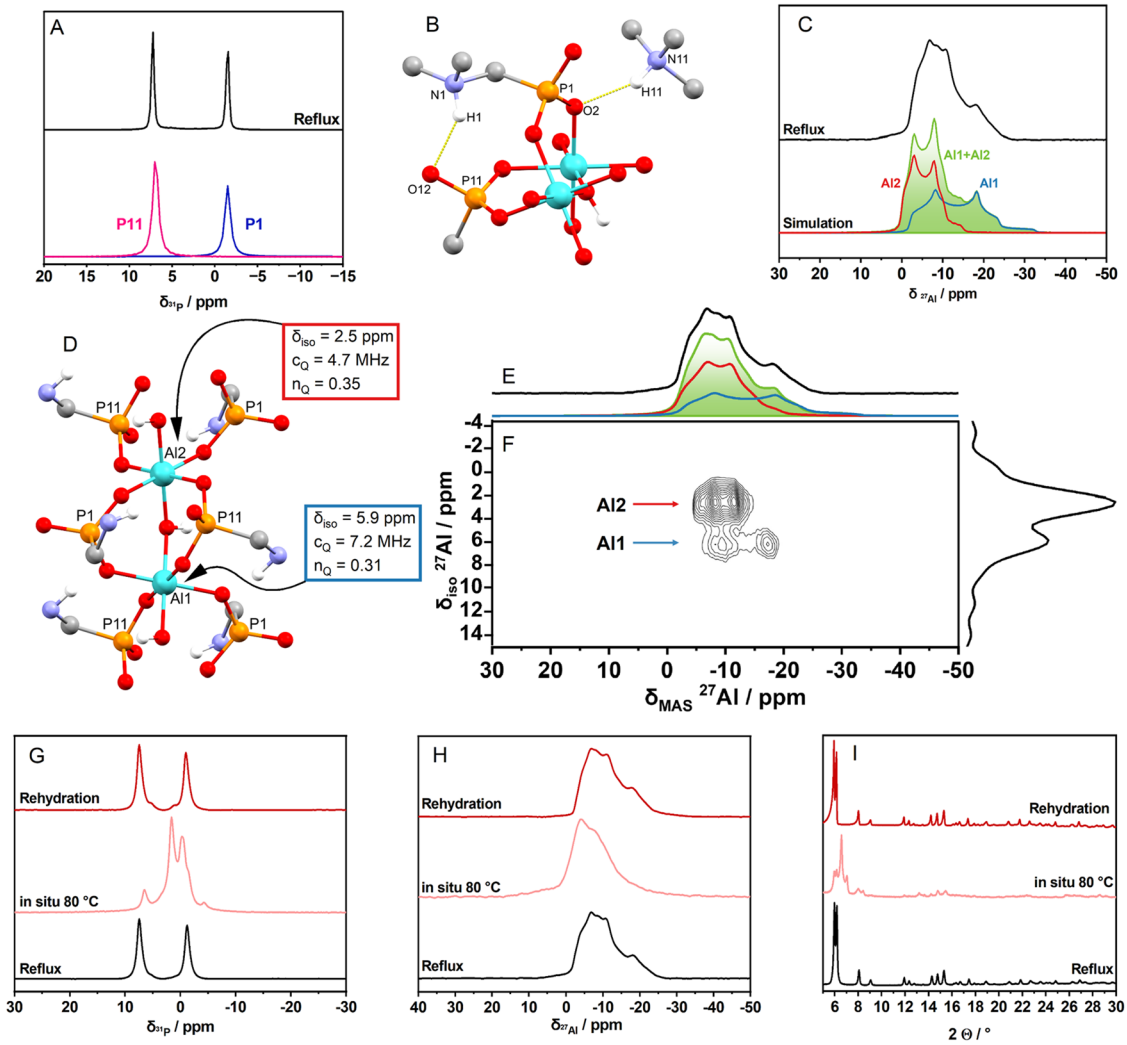

Figure 6. Solid-state NMR and structural characterization of Al-CAU-67. (A) ^{31}P MAS NMR spectrum of Al-CAU-67-Reflux (black) with simulated P1 (blue) and P11 (pink) contributions. (B) Bonding environments of P1 and P11. The single-bonded atom O2, which is connected to P1 and coordinating to Al2, forms a weaker H-bond compared to O12, which forms a double bond to P11. (C) Experimental (black) and DFT-simulated (green, Al1 + Al2) ^{27}Al MAS spectra, with individual Al1 (blue) and Al2 (red) contributions. (D) Local coordination environments of Al1 and Al2 and their quadrupolar parameters. (E) 1D ^{27}Al MAS NMR spectrum of Al-CAU-67 (black) and fitted Al1 (blue), Al2 (red) and the summed contributions (green, Al1 + Al2). (F) ^{27}Al 3Q MAS NMR spectrum of Al-CAU-67. (G, H) ^{31}P MAS NMR and ^{27}Al MAS NMR of Al-CAU-67-Reflux (black), activated Al-CAU-67 at 80 °C under vacuum (light red), and rehydrated Al-CAU-67 after reflux in water for 1 h (red). (I) PXRD data of Al-CAU-67-Reflux (black), activated Al-CAU-67 at 80 °C in situ under vacuum (light red), and rehydrated Al-CAU-67 after reflux in water for 1 h (red).

PoreBlazer.[44−46] The pronounced hysteresis in the N_2 isotherm is likely attributed primarily to slow N_2 diffusion in narrow channels, with possible additional contributions from framework flexibility or delayed pore opening.

Similar results with Ar at 87 K (SI Section 4.7) further indicate that the reduced surface area arises from framework contraction upon activation, consistent with the VT-PXRD results (Figure 3). Water sorption data revealed a maximum uptake of 9 water molecules per formula unit (n_a in mol mol^{-1}; equivalent to 22.6 mmol g^{-1}, Figure 4B) in three distinct steps (two, four, and three molecules), indicative of progressive pore filling and framework flexibility. Kinetic limitations during rehydration are likely to account for the lower uptake observed relative to TG and elemental analysis. The vapor-sorption isotherms of MeOH, EtOH, 1-BuOH, and toluene reflect the impact of the differences in kinetic diameter (3.63,[55] 4.53,[55] 5.0,[56] and 5.25[55] Å) and specific host−guest interactions.

The maximum uptakes reached 12.0 mmol g^{-1} (4.8 mol mol^{-1}) for MeOH, 6.6 mmol g^{-1} (2.6 mol mol^{-1}) for EtOH, 4.6 mmol g^{-1} (1.5 mol mol^{-1}) for 1-BuOH, and 1.9 mmol g^{-1} (0.8 mol mol^{-1}) for toluene (Figure 4). Multistep isotherms, characteristic of adsorption-induced framework flexibility, were observed for H_2O, MeOH, EtOH, and 1-BuOH. Depending on the probe molecule, the secondary uptake step occurred at markedly different relative pressures. For H_2O and EtOH, this step was observed at comparatively low p/p_0 values, whereas for MeOH and 1-BuOH it shifted to higher p/p_0. In contrast, toluene exhibited single-step sorption behavior. We hypothesize that these differences arise from distinct sorbate−sorbent and sorbate−sorbate interactions that either trigger or suppress framework flexibility, depending on the adsorbate. Additional characterization of the sorption behavior, as well as investigation of cyclic sorption with the INFRAsorp method, is provided in SI Section 4.7.

https://doi.org/10.1021/acs.chemmater.6c01336
Chem. Mater. 2026, 38, 8463−8475

Downloaded from pubs.acs.org/cmatex/article-pdf/38/16/8463/66357783/acs.chemmater.6c01336.pdf by IMEC VZW user on 28 October 2026

Solvent-Driven Structure Changes

To investigate the reversible breathing behavior[57−60] upon de- and rehydration, in situ PXRD was conducted under controlled relative humidity (RH) (Figure 5). First, Al-CAU-67-SE was activated under dry N_2 at 80 °C for 3 h. Upon activation, the most prominent reflections shifted to higher 2θ values and broadened, while weaker reflections were attenuated. These changes are consistent with the contraction of the unit cell and a reduced long-range order in the dehydrated framework (SI Section 4.9.1). Subsequently, the sample was exposed to increasing RH levels, corresponding to the steps of the water-vapor isotherm.

At low RH (≤15%), the diffractograms were dominated by reflections of this activated phase, in line with the uptake in the initial p/p_0 (0.0−0.1) regime of the isotherm (Figure 5). Between 15 and 35% RH, the reflections systematically shifted toward lower 2θ values and additional reflections emerged, indicating lattice expansion to accommodate the water molecules. Above 40% RH, the diffraction patterns progressively reverted toward that of the hydrated Al-CAU-67 phase, with a mixed-phase region in the 40−70% RH range in which the dehydrated and hydrated structures, as well as additional intermediate phases, coexist. While the presence of phase mixtures may reflect kinetically hindered hydration, the complete recovery of crystallinity upon rehydration confirms that the transformation is reversible. Exposure of partially hydrated Al-CAU-67 to 75% RH for 30 h or reflux in water for 1 h resulted in complete rehydration and restoration of crystallinity (Figure 5 and SI Section 4.7.5), as observed for Al-MIL-91.[26]

Solid-State NMR Investigation

Further insights into the local coordination environments within Al-CAU-67 were obtained using solid-state NMR spectroscopy (ssNMR). In the ^{31}P MAS NMR spectrum, two sharp and well-resolved resonances were observed (Figure 6A), originating from the structure of Al-CAU-67, which contains two distinct phosphonate groups (Figure 6B). The downfield resonance at 7.5 ppm corresponds to the P11-centered phosphonate group, while the upfield signal at −1 ppm arises from the P1-centered phosphonate. The chemical shift difference is attributed to a weaker hydrogen-bonding nature of the N11−H11···O2−P1 bond, as reflected in its longer donor−acceptor distance (2.844(10) Å vs 2.788(14) Å for N1−H1···O12 = P11). In addition, the latter interaction involves a phosphoryl oxygen (P=O), which typically forms stronger hydrogen bonds than bridging oxygen atoms (P−O−M) (Figure 6B). To support the experimental ssNMR analysis, ab initio DFT simulations based on the proposed structure were performed (SI section 4.8). The calculated contributions of O2−P1 (blue) and O12=P11 (pink) closely match the experimental ^{31}P NMR spectrum, confirming the assignment of these phosphorus environments (Figure 6 B). Following a postsynthetic reflux treatment, the resolution of the ^{31}P resonances increases, which can be attributed to reduced structural disorder resulting in more uniform phosphorus environments (SI Section 4.8.2). Notably, such spectral sharpening is absent in the Al-MIL-91 framework (SI Section 4.8.3). The ^{27}Al MAS NMR spectrum of Al-CAU-67-Reflux exhibited a characteristic second-order quadrupolar line shape, consistent with aluminum in 6-fold-coordinated (octahedral-like) environments (Figure 6C).[47,61] The sum of the DFT-simulated spectra derived from the quadrupolar contour plots of each contribution shows good agreement with the experimental one-dimensional ^{27}Al MAS NMR spectrum (Figure 6C), validating the structural model derived from SCXRD data and PXRD refinements (SI Section 4.8.2). To further resolve the individual Al sites (Figure 6D), ^{27}Al triple-quantum magic-angle spinning (^{27}Al 3Q MAS) spectroscopy was employed (Figure 6E,F). This technique averages the anisotropy of the second-order quadrupolar interaction on the central transition, resolving overlapping quadrupolar resonances in the MAS NMR spectrum. The 3Q MAS spectrum displayed two prominent resonances, confirming the presence of two 6-fold-coordinated (AlO_6) sites, Al1 and Al2 (Figure 6 F). The isotropic signal at around 6 ppm can be attributed to the Al1 site (δ_{iso} = 5.9 ppm, C_Q = 7.2 MHz, η_Q = 0.31; Figure 6D) and correlates with the overall MAS spectrum (from about 0 to −30 ppm). In comparison, the isotropic contribution around 2.5 ppm, assigned to Al2 (δ_{iso} = 2.5 ppm, C_Q = 4.7 MHz, η_Q = 0.35; Figure 6D), specifically correlates with the MAS spectral region from 0 to −15 ppm. The quadrupolar parameters are aligned with the NMR parameters obtained from DFT (SI Section 4.8.2). The C_Q values of both sites are consistent with comparatively symmetric near-octahedral Al environments. The Al1 site exhibits a larger C_Q than Al2, indicating a slightly greater distortion of its octahedral coordination geometry, yet a smaller η_Q, corresponding to a more axially symmetric electric-field gradient.[62]

To probe local structural changes in the flexible Al-CAU-67 framework, ssNMR experiments were performed. The solvent-exchanged sample (Al-CAU-67-SE) was dried under vacuum (<10^{-2} kPa) for 2 h, packed into the rotor under inert atmosphere, and activated in situ at 80 °C inside the NMR spectrometer. The ^{31}P and ^{27}Al ssNMR spectra of the thermally activated material (Figure 6G,H) showed clear changes in the local coordination environment relative to the hydrated state, consistent with the phase transition observed by VT-PXRD under vacuum at 80 °C (Figure 6I). At 80 °C, the ^{31}P MAS NMR spectrum (Figure 6G) exhibited additional signals, indicating reduced framework symmetry or the existence of multiple phases. The changes in the phosphorus environments correlated with modifications at the nitrogen sites, as the phosphonate and tertiary amine groups engage in hydrogen bonding. This hypothesis is supported by XPS analysis of the N 1s region, which revealed that only ∼60% of nitrogen sites remained protonated under high-vacuum conditions, indicating weakened hydrogen bonding and increased linker flexibility upon partial dehydration (SI Section 4.12).

Similarly, the ^{27}Al NMR spectra at 80 °C (Figure 6H) showed changes that predominantly affect the Al1 site, consistent with a decrease in quadrupolar coupling at this site. Site-selective assignment was achieved by comparison with NMR simulations of the hydrated phase, which distinguished the contributions from Al1 and Al2. Upon thermal activation, the signals associated with Al1 were perturbed, whereas those from the Al2-site remained largely unchanged.

The reversibility of these structural changes is demonstrated by subjecting the activated material to a 1 h reflux treatment in water, which restored both the ^{27}Al and ^{31}P NMR signatures and the initial diffraction pattern (Figure 6G−I). The ^{27}Al 3Q MAS NMR spectra of the rehydrated sample again resolved

Downloaded from pubs.acs.org/cmatex/article-pdf/38/16/8463/66357783/acs.chemmater.6c01336.pdf by IMEC VZW user on 28 October 2026

https://doi.org/10.1021/acs.chemmater.6c01336
Chem. Mater. 2026, 38, 8463−8475

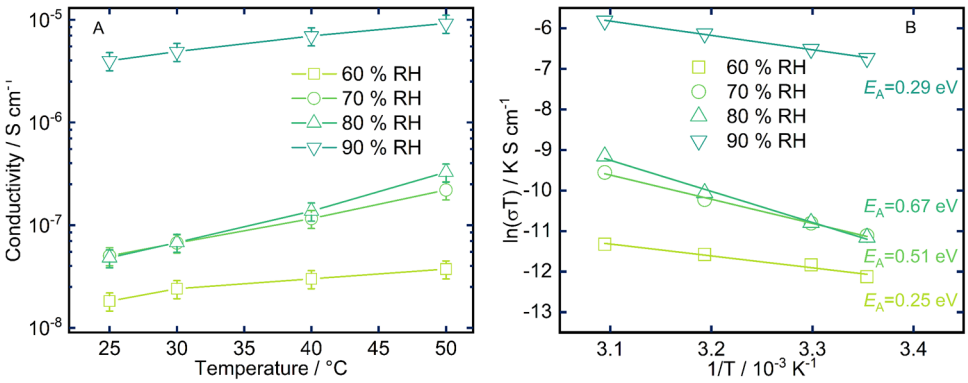

Figure 7. (A) Proton conductivity of Al-CAU-67 at variable relative humidity in a temperature range of 25 to 50 °C. Lines serve as a guide for the eye and have no physical meaning. (B) Arrhenius plots at variable relative humidity with linear fits and calculated activation energies (E_A).

two distinct Al sites, and the quadrupolar parameters are consistent with those of Al-CAU-67-Reflux (SI Section 4.8.2).

Proton Conductivity

The proton conductivity of Al-CAU-67 was investigated using impedance spectroscopy over the frequency range of 1 Hz to 4.61 MHz. The Nyquist plots shown in the SI Section 4.10 were evaluated by fitting the data with an equivalent circuit consisting of a resistor (R) and a parallel constant-phase element (CPE), with an additional resistor (R') to account for the contact resistance between the sample and the electrodes.[63] Measurements were performed at different temperatures between 25 and 50 °C and at relative humidities between 60 and 90% (Figure 7A). Humidity is known to have a strong impact on proton conductivity.[64] As expected, Al-CAU-67 shows increased conductivity with increasing humidity. At RH of 80% or lower, Al-CAU-67 exhibits low conductivity in the range of 10^{-8} to 10^{-7} S cm^{-1}. Increasing the RH to 90% increases the conductivity by 2 orders of magnitude, reaching values up to 10^{-5} S cm^{-1}. The pronounced increase in conductivity is not directly proportional to the comparatively small additional water uptake in this humidity range. This indicates a threshold-like change in the proton-transport pathway rather than a simple increase in the number of charge carriers. Although RH-PXRD shows that the material remains in the same average crystalline phase, local rearrangements of the pore water and changes in hydrogen-bond connectivity are not resolved by diffraction. The additional water adsorbed at high RH may therefore complete a more dynamically reorientable hydrogen-bond network within the pores, enabling better proton transport. Although Al-CAU-67 contains a large amount of water molecules under humid conditions, the absolute proton conductivity values remain comparatively low. This could be rationalized by the hydrated structural model, in which the water oxygen sites are mainly distributed in the center of the one-dimensional pores rather than along the polar walls of the IBU surface. The high water content, therefore, does not necessarily result in a continuous water chain or percolating hydrogen-bonding pathway. However, the water oxygen sites represent an averaged model of disordered pore water and should not be interpreted as an exact localization of individual water molecules.

To gain insights into the proton-conduction mechanism, temperature-dependent measurements were performed at each RH. The relation between conductivity and temperature was used to estimate the activation energy (E_A) for proton mobility by the Arrhenius eq (Figure 7B). For Al-CAU-67, low activation energies (≤0.3 eV) were observed at 90% RH, which indicates that proton conduction occurs predominantly by a "proton hopping" mechanism, similar to the Grotthuss mechanism in bulk liquid water. This behavior is consistent with a high degree of pore hydration at high relative humidity. At lower relative humidities (70−80% RH), the activation energy increased to ≥0.5 eV, suggesting that proton conduction by mass transport becomes more significant (i.e., by diffusion of H_3O^+). At the lowest relative humidity investigated (60% RH), the activation energy decreased to 0.25 eV, which may result from structural changes that enable the phosphonate and tertiary amine groups to participate in proton transport. The Nyquist plots, as well as the recorded data for Ga-CAU-67, are shown in the SI Section 4.10.

■ CONCLUSIONS

Two phosphonate MOFs, Al- and Ga-CAU-67, [M(OH)-(H_2BPD)] (M = Al^{3+}, Ga^{3+}), which are isoreticular to MIL-91 have been obtained using the linker-extension strategy. In analogy to MIL-91, the lattice is also stabilized by intraframework N−H···O−P hydrogen bonds between tertiary nitrogen atoms and phosphonate groups. In contrast to MIL-91, CAU-67 exhibits complex framework flexibility. The combination of diffraction, sorption, thermal analysis, vibrational, and ssNMR spectroscopy demonstrates that these frameworks undergo a sequence of discrete hydration states in which the removal or uptake of well-defined numbers of water molecules per formula unit drives reversible transformations between hydrated large-pore and dehydrated narrow-pore forms. The multistep water sorption and TG/DSC data rationalize these transitions as successive depletion or filling of hydrogen-bonded water molecules, up to a maximum of about 13 water molecules per formula unit. The large mismatch between the theoretical surface area of the fully expanded structure ($S_{BET,\ theo}$ = 1084 m^2 g^{-1}) and the experimentally accessible BET area (S_{BET} = 205 m^2 g^{-1}) indicates that activation results in a contracted framework. In contrast to the N_2 sorption curve at 77 K, the sorption of polar and protic guests (H_2O, MeOH, EtOH, 1-BuOH) induces framework flexibility, as evidenced by multistep adsorption curves. NMR crystallography resolves two distinct aluminum and phosphorus environments and tracks local flexibility, thereby validating the structural model. Finally, humidity-dependent proton conductivity measurements connect these discrete hydration states to a change in transport mechanism: at high relative humidity, continuous water networks support low-barrier Grotthuss-type hopping,

https://doi.org/10.1021/acs.chemmater.6c01336
Chem. Mater. 2026, 38, 8463−8475

Downloaded from pubs.acs.org/cmatex/article-pdf/38/16/8463/66357783/acs.chemmater.6c01336.pdf by IMEC VZW user on 28 October 2026

while at intermediate and low humidity, disruption of these networks shifts proton conduction first toward mass transport, and at even lower humidities, as the activation energy lowers again, a framework-assisted transport involving phosphonate and tertiary nitrogen atoms occurs. Overall, CAU-67 provides a rare, structurally well-resolved example of isoreticular expansion in phosphonate MOFs, in which structural flexibility, water content, accessible porosity, and proton conduction can all be rationalized within the framework's structure−property relationship.

■ ASSOCIATED CONTENT

Supporting Information

The Supporting Information is available free of charge at https://pubs.acs.org/doi/10.1021/acs.chemmater.6c01336.

> Literature of porous aluminum phosphonates, detailed experimental methods and synthesis description, summary of the HT investigations and synthesis optimization, SCXRD, PXRD, and PDF data, digested liquid NMR data, TG and elemental analysis, DSC, ATR-FTIR, and DRIFTS, SEM images, physisorption and optical calorimetry investigations, Solid-State NMR, VT-PXRD, proton conductivity, stability test, and XPS data (DOCX)

Accession Codes

Deposition Numbers 2452205, 2487365, and 2487454 contain the supplementary crystallographic data for this paper. These data can be obtained free of charge via the joint Cambridge Crystallographic Data Centre (CCDC) and Fachinformationszentrum Karlsruhe Access Structures service.

■ AUTHOR INFORMATION

Corresponding Authors

Wouter Marchal − *Institute for Materials Research (IUMAT), Analytical and Circular Chemistry (ACC), Metabolomics and Advanced Solid-State NMR Group (MAS NMR), Hasselt University, 3500 Hasselt, Belgium;* orcid.org/0000-0001-5105-8112; Email: wouter.marchal@uhasselt.be

Rob Ameloot − *Centre for Membrane Separations, Adsorption, Catalysis, and Spectroscopy (cMACS), KU Leuven (Arenberg), 3001 Leuven, Belgium;* orcid.org/0000-0003-3178-5480; Email: rob.ameloot@kuleuven.be

Norbert Stock − *Institut für Anorganische Chemie, Christian-Albrechts-Universität zu Kiel, 24118 Kiel, Germany;* orcid.org/0000-0002-0339-7352; Email: stock@ac.uni-kiel.de

Authors

Jennifer Theissen − *Centre for Membrane Separations, Adsorption, Catalysis, and Spectroscopy (cMACS), KU Leuven (Arenberg), 3001 Leuven, Belgium; Institute for Materials Research (IUMAT), Analytical and Circular Chemistry (ACC), Metabolomics and Advanced Solid-State NMR Group (MAS NMR), Hasselt University, 3500 Hasselt, Belgium*

Marvin Radke − *Institut für Anorganische Chemie, Christian-Albrechts-Universität zu Kiel, 24118 Kiel, Germany;* orcid.org/0009-0007-7587-9960

Sebastian Mangelsen − *Institut für Anorganische Chemie, Christian-Albrechts-Universität zu Kiel, 24118 Kiel, Germany;* orcid.org/0000-0003-2121-9514

Elien Derveaux − *Institute for Materials Research (IUMAT), Analytical and Circular Chemistry (ACC), Metabolomics and Advanced Solid-State NMR Group (MAS NMR), Hasselt University, 3500 Hasselt, Belgium*

Roberth Mateo Narváez Adams − *General Chemistry (ALGC), Materials Modeling Group, Vrije Universiteit Brussel, 1050 Brussels, Belgium; Department of Materials and Chemistry-Sustainable Materials Engineering (SUME) Research Group of Electrochemical and Surface Engineering (SURF), Vrije Universiteit Brussel, 1050 Brussels, Belgium;* orcid.org/0000-0002-3376-3632

Tobias Wagner − *Department of Chemistry, Paderborn University, 33098 Paderborn, Germany*

Jasper Lopau − *Institut für Anorganische Chemie, Christian-Albrechts-Universität zu Kiel, 24118 Kiel, Germany*

Christian Näther − *Institut für Anorganische Chemie, Christian-Albrechts-Universität zu Kiel, 24118 Kiel, Germany;* orcid.org/0000-0001-8741-6508

Christian Nelle − *Department of Chemistry and Chemical Biology, TU Dortmund, 44227 Dortmund, Germany;* orcid.org/0009-0005-8704-435X

Jörn Struve − *Institut für Anorganische Chemie, Christian-Albrechts-Universität zu Kiel, 24118 Kiel, Germany*

Felix Steinke − *Institut für Anorganische Chemie, Christian-Albrechts-Universität zu Kiel, 24118 Kiel, Germany*

Jesús Gándara Loe − *Centre for Membrane Separations, Adsorption, Catalysis, and Spectroscopy (cMACS), KU Leuven (Arenberg), 3001 Leuven, Belgium;* orcid.org/0000-0003-1334-4788

Nick Gys − *Centre for Membrane Separations, Adsorption, Catalysis, and Spectroscopy (cMACS), KU Leuven (Arenberg), 3001 Leuven, Belgium; Department of Materials and Chemistry-Sustainable Materials Engineering (SUME) Research Group of Electrochemical and Surface Engineering (SURF), Vrije Universiteit Brussel, 1050 Brussels, Belgium*

Tom Hauffman − *Department of Materials and Chemistry-Sustainable Materials Engineering (SUME) Research Group of Electrochemical and Surface Engineering (SURF), Vrije Universiteit Brussel, 1050 Brussels, Belgium*

Michael Tiemann − *Department of Chemistry, Paderborn University, 33098 Paderborn, Germany;* orcid.org/0000-0003-1711-2722

Frederik Tielens − *General Chemistry (ALGC), Materials Modeling Group, Vrije Universiteit Brussel, 1050 Brussels, Belgium;* orcid.org/0000-0002-6760-6176

Peter Adriaensens − *Institute for Materials Research (IUMAT), Analytical and Circular Chemistry (ACC), Metabolomics and Advanced Solid-State NMR Group (MAS NMR), Hasselt University, 3500 Hasselt, Belgium;* orcid.org/0000-0003-4183-0150

Sebastian Henke − *Department of Chemistry and Chemical Biology, TU Dortmund, 44227 Dortmund, Germany;* orcid.org/0000-0003-1502-6038

Complete contact information is available at: https://pubs.acs.org/10.1021/acs.chemmater.6c01336

Author Contributions

○J.T. and M.R. are co-first authors and contributed equally to this work. J.T. and M.R. designed the project and performed

Downloaded from pubs.acs.org/cmatex/article-pdf/38/16/8463/66357783/acs.chemmater.6c01336.pdf by IMEC VZW user on 28 October 2026

formal analysis, conceptualization, data curation, methodology, and investigation; M.R. and J.T. performed the major part of the experimental work, assisted by J.L. and J.S.; J.T., E.D., and P.A. carried out NMR measurements; J.T. and J.G.L. performed VT- and humidity-dependent XRD; C.N. performed SCXRD measurements and refinement; S.M. performed the refinement of PXRD and PDF data; M.R. and F.S. made refinement of PXRD data; R.M.N.A. and F.T. performed simulations; N.G. and T.H. conducted XPS measurements; C.N. and S.H. conducted DTA-TG and DSC investigations; T.W. and M.T. performed proton conductivity measurements; M.R. and J.T. did the visualization. Funding acquisition by N.S., R.A., and W.M. Supervision by N.S., R.A., and W.M. The manuscript was written with contributions from all authors. All authors have approved the final version of the manuscript.

Funding

This work was supported by the Flemish Research Foundation (FWO Vlaanderen) through a travel grant for a long stay abroad at Kiel University (V429124N), the FWO and F.R.S.-FNRS (Belgium) under the Excellence of Science (EOS) program ("PHOSPORE", EOS reference number: 40,007,504), the state of Schleswig-Holstein (Germany), KU Leuven, Hasselt University, and FWO Vlaanderen via the Hercules projects AUHL/15/2 (GOH3816N) and I001324N. The high-resolution SEM with an EDX detector was funded by the Deutsche Forschungsgemeinschaft (DFG) under grant 529613430 (DFGINST 257/717−1 FUGG). The FWO funded the Versaprobe III as part of its medium-scale research infrastructure (I006220N). J.G.L. acknowledges support from the FWO Vlaanderen for his Junior FWO Postdoctoral Fellowship (12E5123N). F.T. acknowledges support from the Vrije Universiteit Brussel (VUB), including a Strategic Research Program awarded to his group.

Notes

The authors declare no competing financial interest.

■ ACKNOWLEDGMENTS

The authors thank the NMR core at Hasselt University (S. Smeets); L. Fusaro for assistance with Simpson simulations; E. Thijssen and N. Ghanemnia for support with ICP measurements; the spectroscopic division of the Department of Inorganic Chemistry at Kiel University (T. Engesser, S. Pehlke, J. Pick, and B. Burghoff) and the NMR division of the Department of Organic Chemistry at Kiel University (F. Sönnichsen, G. Agha, and G. Kohlmeyer-Yilmaz) for support with liquid NMR measurements. We also thank N. Pienack and D. Egawa for support with the SEM images and C. Meier, T. Otto, H. Rohr, and B. Achenbach for help with sorption measurements. We acknowledge the European Synchrotron Radiation Facility (ESRF) for the provision of synchrotron radiation facilities under proposal MA-6553 (DOI: 10.15151/ESRF-ES-2193756500) and C. Dejoie for assistance at beamline ID22 as well as J.G.L., L. Boullart, and L. Meneghin for support during beamtime at ESRF (ID22); N. Ma and the beamline at SPring-8 for the synchrotron X-ray total scattering experiments (JASRI proposal No. 2024B1167).

■ REFERENCES

(1) Furukawa, H.; Cordova, K. E.; O'Keeffe, M.; Yaghi, O. M. The chemistry and applications of metal-organic frameworks. *Science* **2013**, *341* (6149), No. 1230444.

(2) Maurin, G.; Serre, C.; Cooper, A.; Férey, G. The new age of MOFs and of their porous-related solids. *Chem. Soc. Rev.* **2017**, *46* (11), 3104−3107.

(3) *Phosphonate Chemistry, Technology, and Applications*; Elsevier, 2026 DOI: 10.1016/C2024-0-00017-3.

(4) Bao, S.-S.; Shimizu, G. K.; Zheng, L.-M. Proton conductive metal phosphonate frameworks. *Coord. Chem. Rev.* **2019**, *378*, 577−594.

(5) Huang, Y.; Zhou, F.; Feng, J.; Zhao, H.; Qi, C.; Ji, J.; Bao, S.; Zheng, T. An ultra-stable hafnium phosphonate MOF platform for comparing the proton conductivity of various guest molecules/ions. *Chem. Commun.* **2021**, *57* (10), 1238−1241.

(6) Zheng, T.; Yang, Z.; Gui, D.; Liu, Z.; Wang, X.; Dai, X.; Liu, S.; Zhang, L.; Gao, Y.; Chen, L.; Sheng, D.; Wang, Y.; Diwu, J.; Wang, J.; Zhou, R.; Chai, Z.; Albrecht-Schmitt, T. E.; Wang, S. Overcoming the crystallization and designability issues in the ultrastable zirconium phosphonate framework system. *Nat. Commun.* **2017**, *8*, No. 15369.

(7) Salcedo-Abraira, P.; Serrano-Nieto, R.; Biglione, C.; Cabrero-Antonino, M.; Vilela, S. M.; Babaryk, A. A.; Tilve-Martínez, D.; Rodriguez-Diéguez, A.; Navalón, S.; García, H.; Horcajada, P. Two Cu-Based Phosphonate Metal−Organic Frameworks as Efficient Water-Splitting Photocatalysts. *Chem. Mater.* **2023**, *35* (11), 4211−4219.

(8) Gao, C.-Y.; Ai, J.; Tian, H.-R.; Wu, D.; Sun, Z.-M. An ultrastable zirconium-phosphonate framework as bifunctional catalyst for highly active CO2 chemical transformation. *Chem. Commun.* **2017**, *53* (7), 1293−1296.

(9) Xie, H.; Atilgan, A.; Joodaki, F.; Cui, J.; Wang, X.; Chen, H.; Yang, L.; Zhang, X.; Son, F. A.; Idrees, K. B.; Wright, A. M.; Wells, J. L.; Morris, W.; Klein, J.; Franklin, L.; Harrington, F.; Herrington, S.; Han, S.; Kirlikovali, K. O.; Islamoglu, T.; Snurr, R. Q.; Farha, O. K. Hydrolytically Stable Phosphonate-Based Metal-Organic Frameworks for Harvesting Water from Low Humidity Air. *Small* **2025**, *21* (22), No. e2503178.

(10) Ramesha, B. M.; Meynen, V. Advances and Challenges in the Creation of Porous Metal Phosphonates. *Materials* **2020**, *13* (23), No. 5366.

(11) Groom, C. R.; Bruno, I. J.; Lightfoot, M. P.; Ward, S. C. The Cambridge Structural Database. *Acta Crystallogr., Sect. B:Struct. Sci., Cryst. Eng. Mater.* **2016**, *72* (Pt 2), 171−179.

(12) Firmino, A. D. G.; Mendes, R. F.; Figueira, F.; Tomé, J. P. C.; Almeida Paz, F. A. Exceptional thermal stability of lanthanide-phosphonate frameworks. *J. Mater. Chem. C* **2024**, *12* (38), 15401−15407.

(13) Healy, C.; Patil, K. M.; Wilson, B. H.; Hermanspahn, L.; Harvey-Reid, N. C.; Howard, B. I.; Kleinjan, C.; Kolien, J.; Payet, F.; Telfer, S. G.; Kruger, P. E.; Bennett, T. D. The thermal stability of metal-organic frameworks. *Coord. Chem. Rev.* **2020**, *419*, No. 213388.

(14) Gagnon, K. J.; Perry, H. P.; Clearfield, A. Conventional and unconventional metal-organic frameworks based on phosphonate ligands: MOFs and UMOFs. *Chem. Rev.* **2012**, *112* (2), 1034−1054.

(15) Shearan, S. J.; Stock, N.; Emmerling, F.; Demel, J.; Wright, P. A.; Demadis, K. D.; Vassaki, M.; Costantino, F.; Vivani, R.; Sallard, S.; Salcedo, I. R.; Cabeza, A.; Taddei, M. New Directions in Metal Phosphonate and Phosphinate Chemistry. *Crystals* **2019**, *9* (5), No. 270.

(16) Patzschke, C.; Forsyth, C. M.; Batten, S. R.; Chaffee, A. L. Formation of a non-porous cobalt-phosphonate framework by small pH change in the preparation of the microporous STA-16(Co). *CrystEngComm* **2014**, *16* (28), 6296−6299.

(17) Zheng, T.; Tan, W.; Zheng, L.-M. Porous Metal Phosphonate Frameworks: Construction and Physical Properties. *Acc. Chem. Res.* **2024**, *57* (20), 2973−2984.

(18) Ondrušová, S.; Kloda, M.; Rohlíček, J.; Taddei, M.; Zaręba, J. K.; Demel, J. Exploring the Isoreticular Continuum between Phosphonate- and Phosphinate-Based Metal-Organic Frameworks. *Inorg. Chem.* **2022**, *61* (47), 18990−18997.

(19) Le Bideau, J.; Payen, C.; Palvadeau, P.; Bujoli, B. Preparation, Structure, and Magnetic Properties of Copper(II) Phosphonates. *β*-

Downloaded from pubs.acs.org/cmatex/article-pdf/38/16/8463/66357783/acs.chemmater.6c01336.pdf by IMEC VZW user on 28 October 2026

Cu^{II}(CH3PO3), an Original Three-Dimensional Structure with a Channel-Type Arrangement. *Inorg. Chem.* **1994**, *33* (22), 4885−4890.
(20) Bonavia, G.; Zubieta, J.; Haushalter, R. C.; O'Connor, C. J.; Sangregorio, C. Hydrothermal synthesis and structural characterization of a tubular oxovanadium organophosphonate, (H3O)-[(V3O4)(H2O)(PhPO3)3]·xH2O(x = 2.33). *Chem. Commun.* **1998**, No. 20, 2187−2188.
(21) Maeda, K.; Akimoto, J.; Kiyozumi, Y.; Mizukami, F. Syntheses and crystal structures of two "organozeolites". In *Progress in Zeolite and Microporous Materials, Preceedings of the 11th International Zeolite Conference*; Elsevier, 1997; pp 197−204 DOI: 10.1016/S0167-2991(97)80556-3.
(22) Alberti, G.; Costantino, U.; Marmottini, F.; Vivani, R.; Zappelli, P. Zirconimphosphit-(3,3′5,5′-tetramethylbiphenyl)diphosphonat: ein mikroporöses anorganisch-organisches Polymer Mit Säulen-Schichtstruktur. *Angew. Chem.* **1993**, *105* (9), 1396−1398.
(23) Dines, M. B.; Cooksey, R. E.; Griffith, P. C.; Lane, R. H. Mixed-component layered tetravalent metal phosphonates/phosphates as precursors for microporous materials. *Inorg. Chem.* **1983**, *22* (6), 1003−1004.
(24) Ghanemnia, N.; Saitta, M.; Derveaux, E.; Tomer, R.; Gys, N.; Hauffman, T.; Adriaensens, P.; Hermans, S.; Aprile, C.; Marchal, W. Zirconium (IV) layered phosphonate-phosphate as catalysts for the valorization of glycerol. *Front. Chem.* **2026**, *13*, No. 1735925.
(25) Alberti, G.; Vivani, R.; Marmottini, F.; Zappelli, P. Microporous Solids Based on Pillared Metal(IV) Phosphates and Phosphonates. *J. Porous Mater.* **1998**, *5* (3/4), 205−220.
(26) Serre, C.; Groves, J. A.; Lightfoot, P.; Slawin, A. M. Z.; Wright, P. A.; Stock, N.; Bein, T.; Haouas, M.; Taulelle, F.; Férey, G. Synthesis, Structure and Properties of Related Microporous N, N′-Piperazinebismethylenephosphonates of Aluminum and Titanium. *Chem. Mater.* **2006**, *18* (6), 1451−1457.
(27) Llewellyn, P. L.; Garcia-Rates, M.; Gaberová, L.; Miller, S. R.; Devic, T.; Lavalley, J.-C.; Bourrelly, S.; Bloch, E.; Filinchuk, Y.; Wright, P. A.; Serre, C.; Vimont, A.; Maurin, G. Structural Origin of Unusual CO 2 Adsorption Behavior of a Small-Pore Aluminum Bisphosphonate MOF. *J. Phys. Chem. C* **2015**, *119* (8), 4208−4216.
(28) Wharmby, M. T.; Mowat, J. P. S.; Thompson, S. P.; Wright, P. A. Extending the pore size of crystalline metal phosphonates toward the mesoporous regime by isoreticular synthesis. *J. Am. Chem. Soc.* **2011**, *133* (5), 1266−1269.
(29) Steinke, F.; Javed, A.; Wöhlbrandt, S.; Tiemann, M.; Stock, N. New isoreticular phosphonate MOFs based on a tetratopic linker. *Dalton Trans.* **2021**, *50* (38), 13572−13579.
(30) Reichenau, T. M.; Steinke, F.; Wharmby, M. T.; Näther, C.; Engesser, T. A.; Stock, N. Targeted Synthesis of a Highly Stable Aluminium Phosphonate Metal-Organic Framework Showing Reversible HCl Adsorption. *Angew. Chem., Int. Ed.* **2023**, *62* (26), No. e202303561.
(31) Glavinović, M.; Perras, J. H.; Gelfand, B. S.; Lin, J.-B.; Spasyuk, D. M.; Zhou, W.; Shimizu, G. K. H. Microporous Metal-Phosphonates with a Novel Orthogonalized Linker and Complementary Guests: Insights for Trivalent Metal Complexes from Divalent Metal Complexes. *Chemistry* **2023**, *29* (17), No. e202203835.
(32) Gelfand, B. S.; Huynh, R. P. S.; Mah, R. K.; Shimizu, G. K. H. Mediating Order and Modulating Porosity by Controlled Hydrolysis in a Phosphonate Monoester Metal-Organic Framework. *Angew. Chem., Int. Ed.* **2016**, *55* (47), 14614−14617.
(33) Yaghi, O. M.; O'Keeffe, M.; Ockwig, N. W.; Chae, H. K.; Eddaoudi, M.; Kim, J. Reticular synthesis and the design of new materials. *Nature* **2003**, *423* (6941), 705−714.
(34) Freund, R.; Canossa, S.; Cohen, S. M.; Yan, W.; Deng, H.; Guillerm, V.; Eddaoudi, M.; Madden, D. G.; Fairen-Jimenez, D.; Lyu, H.; Macreadie, L. K.; Ji, Z.; Zhang, Y.; Wang, B.; Haase, F.; Wöll, C.; Zaremba, O.; Andreo, J.; Wuttke, S.; Diercks, C. S. 25 Years of Reticular Chemistry. *Angew. Chem., Int. Ed.* **2021**, *60* (45), 23946−23974.
(35) Shimizu, G. K. H.; Vaidhyanathan, R.; Taylor, J. M. Phosphonate and sulfonate metal organic frameworks. *Chem. Soc. Rev.* **2009**, *38* (5), 1430−1449.
(36) Gagnon, K. J.; Teat, S. J.; Beal, Z. J.; Embry, A. M.; Strayer, M. E.; Clearfield, A. Isoreticular Investigation into the Formation of Four New Zinc Alkylbisphosphonate Families. *Cryst. Growth Des.* **2014**, *14* (7), 3612−3622.
(37) del Mar Gómez-Alcántara, M.; Cabeza, A.; Moreno-Real, L.; Aranda, M. A.; Clearfield, A. Microporous aluminum bisphosphonates. *Microporous Mesoporous Mater.* **2006**, *88* (1−3), 293−303.
(38) Harvey, H. G.; Herve, A. C.; Hailes, H. C.; Attfield, M. P. Synthesis, Crystal Structures, and Modifications of Novel Framework Gallium Diphosphonates. *Chem. Mater.* **2004**, *16* (19), 3756−3766.
(39) Tholen, P.; Zorlu, Y.; Beckmann, J.; Yücesan, G. Probing Isoreticular Expansions in Phosphonate MOFs and their Applications. *Eur. J. Inorg. Chem.* **2020**, *2020* (17), 1542−1554.
(40) Coelho, A. A. Whole-profile structure solution from powder diffraction data using simulated annealing. *J. Appl. Crystallogr.* **2000**, *33* (3), 899−908.
(41) Coelho, A. A. TOPAS and TOPAS-Academic: an optimization program integrating computer algebra and crystallographic objects written in C++. *J. Appl. Crystallogr.* **2018**, *51* (1), 210−218.
(42) Hermer, N.; Wharmby, M. T.; Stock, N. Re-Determination of the Crystal Structure of MIL-91(Al). *Z. Anorg. Allg. Chem.* **2017**, *643* (2), 137−140.
(43) Coxall, R. A.; Harris, S. G.; Henderson, D. K.; Parsons, S.; Tasker, P. A.; Winpenny, R. E. P. Inter-ligand reactions: in situ formation of new polydentate ligands. *Dalton Trans.* **2000**, No. 14, 2349−2356.
(44) Sarkisov, L.; Bueno-Perez, R.; Sutharson, M.; Fairen-Jimenez, D. Materials Informatics with PoreBlazer v4.0 and the CSD MOF Database. *Chem. Mater.* **2020**, *32* (23), 9849−9867.
(45) Sarkisov, L.; Harrison, A. Computational structure characterisation tools in application to ordered and disordered porous materials. *Mol. Simul.* **2011**, *37* (15), 1248−1257.
(46) Sarkisov, L.; Kim, J. Computational structure characterization tools for the era of material informatics. *Chem. Eng. Sci.* **2015**, *121*, 322−330.
(47) Loiseau, T.; Serre, C.; Huguenard, C.; Fink, G.; Taulelle, F.; Henry, M.; Bataille, T.; Férey, G. A rationale for the large breathing of the porous aluminum terephthalate (MIL-53) upon hydration. *Chemistry* **2004**, *10* (6), 1373−1382.
(48) Millange, F.; Walton, R. I. MIL-53 and its Isoreticular Analogues: a Review of the Chemistry and Structure of a Prototypical Flexible Metal-Organic Framework. *Isr. J. Chem.* **2018**, *58* (9−10), 1019−1035.
(49) Cheetham, A. K.; Rao, C. N. R.; Feller, R. K. Structural diversity and chemical trends in hybrid inorganic-organic framework materials. *Chem. Commun.* **2006**, No. 46, 4780−4795.
(50) Taddei, M.; Costantino, F.; Vivani, R. Synthesis and crystal structure from X-ray powder diffraction data of two zirconium diphosphonates containing piperazine groups. *Inorg. Chem.* **2010**, *49* (20), 9664−9670.
(51) Levenson, D. A.; Zhang, J.; Szell, P. M. J.; Bryce, D. L.; Gelfand, B. S.; Huynh, R. P. S.; Fylstra, N. D.; Shimizu, G. K. H. Effects of Secondary Anions on Proton Conduction in a Flexible Cationic Phosphonate Metal−Organic Framework. *Chem. Mater.* **2020**, *32* (2), 679−687.
(52) Fuchs, A.; Knechtel, F.; Wang, H.; Ji, Z.; Wuttke, S.; Yaghi, O. M.; Ploetz, E. Water Harvesting at the Single-Crystal Level. *J. Am. Chem. Soc.* **2023**, *145* (26), 14324−14334.
(53) Hadjiivanov, K. I.; Panayotov, D. A.; Mihaylov, M. Y.; Ivanova, E. Z.; Chakarova, K. K.; Andonova, S. M.; Drenchev, N. L. Power of Infrared and Raman Spectroscopies to Characterize Metal-Organic Frameworks and Investigate Their Interaction with Guest Molecules. *Chem. Rev.* **2021**, *121* (3), 1286−1424.
(54) Rouquerol, F. *Adsorption by Powders and Porous Solids:Principles, Methodology and Applications*, 2nd ed.; Elsevier/Academic Press, 2014.

Downloaded from pubs.acs.org/cmatex/article-pdf/38/16/8463/66357783/acs.chemmater.6c01336.pdf by IMEC VZW user on 28 October 2026

(55) Li, J.-R.; Kuppler, R. J.; Zhou, H.-C. Selective gas adsorption and separation in metal-organic frameworks. *Chem. Soc. Rev.* **2009**, *38* (5), 1477−1504.
(56) Wu, H.; Gong, Q.; Olson, D. H.; Li, J. Commensurate adsorption of hydrocarbons and alcohols in microporous metal organic frameworks. *Chem. Rev.* **2012**, *112* (2), 836−868.
(57) Alhamami, M.; Doan, H.; Cheng, C.-H. A Review on Breathing Behaviors of Metal-Organic-Frameworks (MOFs) for Gas Adsorption. *Materials* **2014**, *7* (4), 3198−3250.
(58) Henke, S.; Schneemann, A.; Wütscher, A.; Fischer, R. A. Directing the breathing behavior of pillared-layered metal-organic frameworks via a systematic library of functionalized linkers bearing flexible substituents. *J. Am. Chem. Soc.* **2012**, *134* (22), 9464−9474.
(59) Murdock, C. R.; Hughes, B. C.; Lu, Z.; Jenkins, D. M. Approaches for synthesizing breathing MOFs by exploiting dimensional rigidity. *Coord. Chem. Rev.* **2014**, *258−259*, 119−136.
(60) Rambabu, D.; Goossens, T.; Bakuru, V. R.; Apostol, P.; Mairesse, F.; Steenhaut, T.; Beaujean, P.; Mondal, S. K.; Guo, X.; Zhang, Y.; Pal, S.; Markowski, R.; Lin, X.; Xu, P.; Chanteux, G.; Kachmar, A.; Da, Tie.; Ramackers, A.; Frano, V.; Robeyns, K.; Kumar Maji, T.; Filinchuk, Y.; Champagne, B.; Vlad, A. Mixed proton-electron conductivity in a dynamic 3D metal-organic framework. *Chem* **2025**, *11*, No. 102590.
(61) Machac, P.; Alauzun, J. G.; Styskalik, A.; Debecker, D. P.; Mutin, P. H.; Pinkas, J. Synthesis of high surface area aluminophosphate and -phosphonate xerogels by non-hydrolytic sol-gel reactions. *Microporous Mesoporous Mater.* **2021**, *311*, No. 110682.
(62) Ashbrook, S. E.; Duer, M. J. Structural information from quadrupolar nuclei in solid state NMR. *Concepts Magn. Reson., Part A* **2006**, *28A* (3), 183−248.
(63) Javed, A.; Steinke, F.; Wöhlbrandt, S.; Bunzen, H.; Stock, N.; Tiemann, M. The role of sulfonate groups and hydrogen bonding in the proton conductivity of two coordination networks. *Beilstein J. Nanotechnol.* **2022**, *13*, 437−443.
(64) Lim, D.-W.; Kitagawa, H. Proton Transport in Metal-Organic Frameworks. *Chem. Rev.* **2020**, *120* (16), 8416−8467.

Downloaded from pubs.acs.org/cmatex/article-pdf/38/16/8463/66357783/acs.chemmater.6c01336.pdf by IMEC VZW user on 28 October 2026

https://doi.org/10.1021/acs.chemmater.6c01336
Chem. Mater. 2026, 38, 8463−8475